Journal of Molecular Liquids 390 (2023) 123192

Contents lists available at ScienceDirect

Journal of Molecular Liquids

journal homepage: www.elsevier.com/locate/molliq

A joint experimental and theoretical study on Structural, Vibrational and morphological properties of newly synthesized nanocomposites involving Hydroxyapatite-alt-Polyethylene Glycol (HAP/PEG)

Dorsaf Bouazzi [a], Imen Chérif [b], Afef Mehri [a], Houcine Touati [c], Maria Teresa Caccamo [d,*], Salvatore Magazù [d], Sahbi Ayachi [b], Jean-Marc Clacens [c], Bechir Badraoui [a]

[a] Laboratory of Condensed Matter and Nanosciences, Faculty of Sciences of Monastir, University of Monastir, Tunisia
[b] Laboratory of Physico-Chemistry of Materials (LR01ES19), Faculty of Sciences, Avenue of the Environment 5019 Monastir, University of Monastir, Tunisia
[c] Institute of Chemistry of Environments and Materials of Poitiers, UMR 7285, ENSI Poitiers, University of Poitiers-CNRS, 4 rue Michel Brunet, BP633, CEDEX, 86022 Poitiers, France
[d] Dipartimento di Scienze Matematiche e Informatiche, Scienze Fisiche e Scienze della Terra Università di Messina, Viale Ferdinando Stagno D'Alcontres n°31, S. Agata, 98166 Messina, Italy

ARTICLE INFO

Keywords:
Hydroxyapatite
Polyethylene glycol
Nanocomposite
XRD
Raman
DFT Calculation

ABSTRACT

In this paper, we report the synthesis and characterization of new nanocomposite materials based on hydroxyapatite (HAP) and polyethylene glycol (PEG) with two different ratios (80/20 and 60/20). The structural properties of the synthesized nanocomposite (HAP/PEG) compound based on chemical composition and morphological features of the surface were analyzed using advanced techniques including X-ray diffraction (XRD), Fourier transform infrared (FT-IR) spectroscopy, Raman spectroscopy and scanning electron microscopy-Energy dispersive spectroscopy (SEM-EDS), which all confirmed the formation of the composite. Furthermore, density functional theory (DFT) computational codes are used, in practice, to predict the structural, optoelectronic properties and quantum chemical parameters of the synthesized nanocomposite compounds. Our results revealed that the nanostructured composite materials containing the fragile HAP (with a weak hardness value) and the rigid PEG (with a strong hardness value) led to the development of a novel nanocomposite material exhibiting improved hardness compared to pure HAP. Moreover, the HAP/PEG nanocomposite exhibited a high level of molecular stability.

1. Introduction

Hydroxyapatite (HAP) has a chemical formula $Ca_{10}(PO_4)_6(OH)_2$ [1] and belongs to the crystallographic family of apatite, which has a general formula of $Me_{10}(XO_4)_6(Y)_2$. This family consists of isomorphic inorganic compounds with the same hexagonal structure. Me typically represents a bivalent cation (such as Ca^{2+}, Mg^{2+}, or Zn^{2+}), XO_4 is a trivalent anionic group (such as PO_4^{3-}, VO_4^{3-}, or AsO_4^{3-}), and Y can be an anion or a monovalent ionic group (such as OH^-, Cl^-, or F^-) [2,3]. HAP is a natural ceramic material with numerous advantages, including high biocompatibility [4], non-toxicity [5], bioactivity, bioresorbability [6,7], and osteoinductivity, osteoconductivity, and osteointegration[8]. Fig. 1 reports the structure of Hydroxyapatite (a) and the structure of polyethyelene glycol (b).

Recently, researchers have attempted to improve and develop specific materials and properties using various types of molecules (such as polymers, acids, and organic matter) that have great potential for various medical applications. These applications include repairing bone defects in orthopedic sites, immediate tooth replacement, augmentation of alveolar ridges, pulp capping materials, and maxillofacial reconstruction [9]. HAP can be integrated with polymers to form composites, which can enhance the expected compatibility by aggregating nanoparticles [10].

The incorporation of organic and/or polymer molecules into the inorganic structure makes it possible to obtain hybrid and multifunctional materials exhibiting synergistic interactions between the two inorganic–organic domains. Recently, research has highlighted the benefits and applications of novel inorganic/polymeric materials,

* Corresponding author.
E-mail address: mcaccamo@unime.it (M. Teresa Caccamo).

https://doi.org/10.1016/j.molliq.2023.123192
Received 5 August 2023; Received in revised form 22 September 2023; Accepted 25 September 2023
Available online 27 September 2023

particularly in tissue engineering and regenerative medicine. In this context, hydroxyapatite (HAP) can be functionalized by organic and/or polymeric molecules to improve these properties such as its mechanical strength, its biocompatibility, or its drug release capacity. Similarly, hybrid hydroxyapatite materials can be used to create surface coatings that promote bone regeneration. HAP-polymers are used in the manufacture of bone implants, surface coatings for prosthetics, matrices for bone regeneration, and carriers for controlled drug release [11]. These hybrid materials provide better integration with surrounding tissues, promote bone growth, and reduce the risk of rejection or inflammation [12]. In recent years, the modification of hydroxyapatite surface by polymers has been increasing and still been under exploration for selected polymers with very advanced biomedical applications [13].

Polyethylene glycol (PEG) is a linear polymer of ethylene oxide with a terminal hydroxyl group that belongs to the family of polyethers. PEG is a water-soluble, non-ionic, neutral, and well-known biocompatible polymer [14]. It is also a biodegradable polymer [15], a hydrophilic polymer, flexible, and nontoxic [16]. PEG is also widely used in numerous fields such as biomedical applications, due to its desirable properties [17].

HAP can be combined with biopolymers, such as Polyethylene Glycol (PEG), due to the action of the polymer aggregating nanoparticles [18]. The combination of PEG with hydroxyapatite can improve the mechanical properties and biocompatibility of the material, making it useful for a variety of biomedical applications.

In this study, HAP/PEG nanocomposites were synthesized using a simple and low-cost method. These nanocomposites were characterized by XRD, ATR-FTIR, Raman Scattering and SEM analysis. Thus, density functional theory (DFT) studies can complement experimental investigations. Herein, the molecular geometry, optimized parameters and vibrational frequencies are computed and the accuracy of the computational methods for DFT//B3LYP/6–31 g(d,p) and ab initio (HF) with 3-21G basis set, are compared.

2. Materials and methods

2.1. Materials

Diammonium hydrogen phosphate ($(NH_4)_2HPO_4$, 98% purity) and calcium nitrate tetrahydrate ($Ca(NO_3)_2{\cdot}4H_2O$, 99% purity) were purchased from Fluka and Sigma, respectively. Ammonia solution ($NH_3{\cdot}H_2O$, 35% purity) was obtained from Prolabo. Polyethylene glycol (PEG, MW = 600) was purchased from Aldrich-Chemie.

2.2. Preparation of hydroxyapatite (HAP) and HAP/PEG compounds

The pure hydroxyapatite was prepared using the co-precipitation method. In nitrogen flux described by Bouazzi et al. [19], under nitrogen flux, an aqueous solution containing 1.67 mol of $Ca(NO_3)_2{\cdot}4H_2O$ was added a one mole of $(NH_4)_2HPO_4$. The pH value of the solution was maintained at 11 by addition of ammonia. The mixture was stirred and heated under reflux at 80 °C. After 3 h, the precipitate was filtered and thoroughly washed with deionized water. The solid was dried at 100 °C overnight.

The synthesis of hydroxyapatite/polyethylene glycol nanocomposites (HAP/PEG) was performed using two weight ratios 80/20 and 60/40 referring to HAP. Firstly, hydroxyapatite (HAP) and polyethylene glycol (PEG) were mixed and dissolved in aqueous solution in a beaker. The mixture was then stirred at 700 rpm for 3 h. After 24 h, the obtained solution was filtered and washed with deionized water until pH 7. Finally, drying at 80 °C was carried out for 24 h.

2.3. Techniques

The structure of the samples was analyzed by X-ray diffraction (XRD) using a Bruker AXS (D 76,187 Karlsruhe, Germany) with Cu-Kα1 radiation (λ = 1.54 Å). The ATR-FTIR technique and Raman spectroscopy were both used in conjunction to characterize the vibrational behavior of the samples. HAP and HAP/PEG nanocomposite were characterized using a Bruker Optics Vertex 80 V FTIR spectrometer in the range of 4000–400 cm^{-1}. Data processing was carried out using the OPUS/Mentor software interface. Raman spectral measurements were carried out on synthesized samples using a HORIBA Jobin-Yvon T64000 spectrometer. He-Ne laser (power: 60 mW; wavelength: 632.8 nm) served as the source. The investigated spectral range was 400–3200 cm^{-1} with varying resolution (from 0.2 to 4 cm^{-1}). The samples were exposed to the laser for 30 s. All experiments were performed at room temperature. The morphology of the samples was analyzed by means of scanning electron microscopy with energy-dispersive X-ray spectroscopy (SEM-EDS) using an INSPECT S instrument (Product version 3.1.2, Build number 843).

2.4. Modelling of the HAP/PEG nanocomposite

Apart from the diverse experimental analysis methods employed to examine the novel HAP/PEG composite and related properties, a complement theoretical calculations based on density functional theory (DFT) [20] using the Becke three-parameter Lee-Yang-Parr (B3LYP) functional [21,22] with basis set 6-31G (d,p) were conducted in this study. This is to predict the structural and vibrational available measurements, as well as to understand the structure–property relationships of the formed nanocomposite including optoelectronic properties and quantum chemical parameters related to its chemical reactivity. Through this analysis, we were also able to determine the geometric properties, specifically the bond lengths and dihedral angles. For the sake of comparison, calculations were performed at the ab-initio Hartree Fock level [22] with the 3-21G basis set.

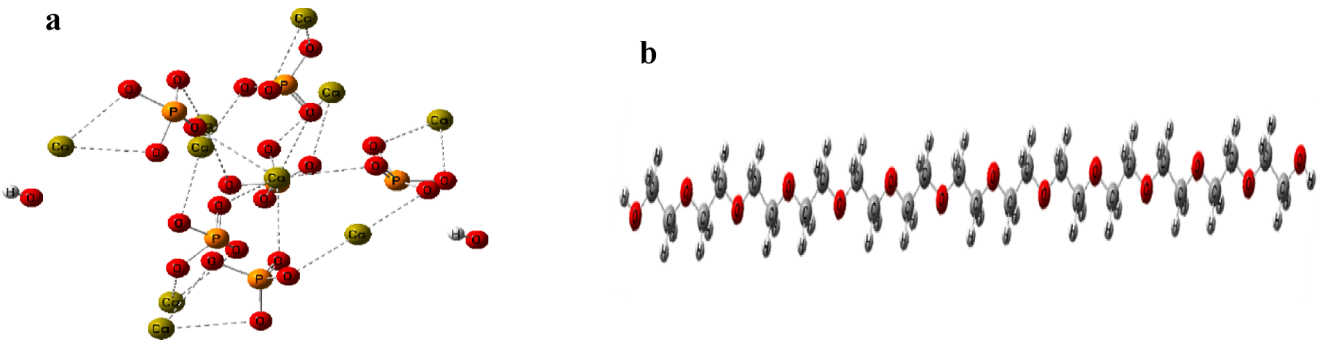

Fig. 1. (a) Structure of Hydroxyapatite (HAP), (b) structure of polyethylene glycol (PEG).

3. Result and discussion

3.1. Structural and vibrational properties of studied samples

The XRD patterns of HAP and HAP/PEG materials are shown in Fig. 2. It shows the characteristic peaks of the apatite structure without secondary phase. The average size of the crystallites was determined by assessing the (002) and (300) prominent peaks, employing Scherer's formula $\mathbf{D_{hkl}} = \mathbf{K}\lambda/\beta_{1/2}\mathbf{cos}\theta$, where θ is the diffraction angle, λ is the wavelength, K a crystal-dependent constant (K = 0.89 for apatite crystallites) and $\beta_{½}$ is to the full width at half maximum (FWHM).

Increasing amounts of ethylene glycol decreased crystallinity, which suggested a decrease in the size of the crystallites. The empirical relationship $\chi_c = \sqrt[3]{\frac{K_A}{\beta_{1/2}}}$ was used to determine the degree of crystallinity (χ_c), where K_A is a constant ($K_A = 0.24$) and $\beta_{½}$ represents the FWHM of the (002) reflection. The obtained results have been documented in Table 1.

It should be highlighted that the incorporation of ethylene glycol slightly broadened the diffraction lines and significantly reduced the crystallinity in comparison with HAP. This occurrence can be elucidated by the existence of preferential interactions between the PEG groups and the HAP surface Ca^{2+}. These interactions, usually electrostatic type, are established between Ca^{2+} ions and the hydroxyl (HO^-) groups of PEFG (Ca^{2+}——$^-$OH). This phenomenon was observed in similar research's [19].

Fig. 3 illustrates the FTIR spectrums of pure HAP, PEG and HAP/PEG mixtures with ratios of 80/20 and 60/40. The characteristic phosphate groups are observed in all samples, appearing between 900 and 1100 cm^{-1} and 550–600 cm^{-1}. Notably, the intensity of the phosphate peaks decreases in the HAP/PEG composites, suggesting a composite structure consisting of β-sheet crystallites embedded within an amorphous matrix [23]. In addition, bands with low vibrational intensities at approximately 3563 cm^{-1} and 630 cm^{-1} can be attributed to the presence of OH groups. Both the 80/20 and 60/40 samples exhibit new bands at 1457 cm^{-1} after HAP has been functionalized; these bands correspond to the stretching vibration of C–H in PEG [24]. Two additional weak peaks at 1714 cm^{-1} and 1757 cm^{-1} indicate the presence of the carbonyl (C = O) group and the (C-O) stretching band of PEG, respectively. These peaks probably arise from the strong electrostatic attraction between the negatively charged C-O-C groups of PEG, which promotes covalent bonds formation with abundant Ca^{2+} ions. The structural characterization conducted through ATR-FTIR was further validated using Raman spectroscopy, an effective analytical technique that provides insights into the molecular structure of materials. Fig. 4 illustrates the Raman spectrum, wherein the prominent peak at approximately 961 cm^{-1} corresponds to the skeletal stretching mode of PO_4^{3-}. Notably, this peak represents a perfectly symmetric stretching mode (v_1: P-O) of the PO4 tetrahedral group [25]. Additionally, lower intensity peaks can be observed, indicating the symmetric bending (v_2: O-P-O) around 430–450 cm^{-1}, antisymmetric bending (v_4: O-P-O) around 580–610 cm^{-1}, and antisymmetric stretching (v_3: P-O)) of the phosphate ions at approximately 1030–1070 cm^{-1} [26].

Table1
Crystallite size and crystallinity for HAP and HAP/PEG.

	$\beta_{(002)}$	D (002) (Å)	$\beta_{(310)}$	D (310) (Å)	χ_c
HAP	0.197	412	0.305	276	1.793
80/20	0.239	341	0.576	146	1.012
60/40	0.274	297	0.637	132	0.671

In terms of polyethylene glycol (PEG), its distinctive peak arises from the symmetric stretching vibrations of the methylene group, observed at 2887 cm^{-1}. The antisymmetric stretching vibration of the methylene group is observed at 2949 cm^{-1}. The band at 1469 cm^{-1} corresponds to the symmetric bending mode of the CH_2-CH_2 group, while the bands at 1241 and 1296 cm^{-1} represent CH_2 twisting vibrations. Furthermore, the C-O stretching and CH_2 rocking vibrations are evident at 1138 and 1047 cm^{-1}, respectively, and the skeletal vibrations of PEG are observed at 836 and 886 cm^{-1} [27].

Raman spectroscopy of the HAP/PEG composite affirms the preservation of phosphate groups within the HAP structure, despite the emergence of a new peak at 1296 cm^{-1} upon the addition of PEG. This new peak suggests the formation of a new chemical species, potentially associated with the vibrational mode of the CH_2 stretching in PEG, indicating the presence of PEG on the surface of hydroxyapatite. This

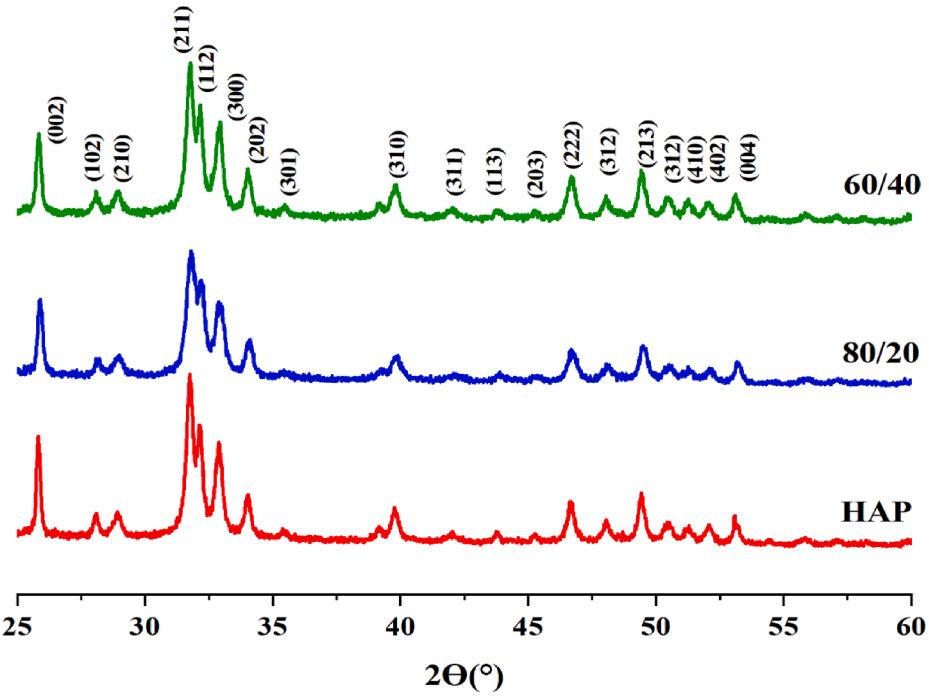

Fig. 2. X-ray diffractograms of HAP and HAP/PEG.

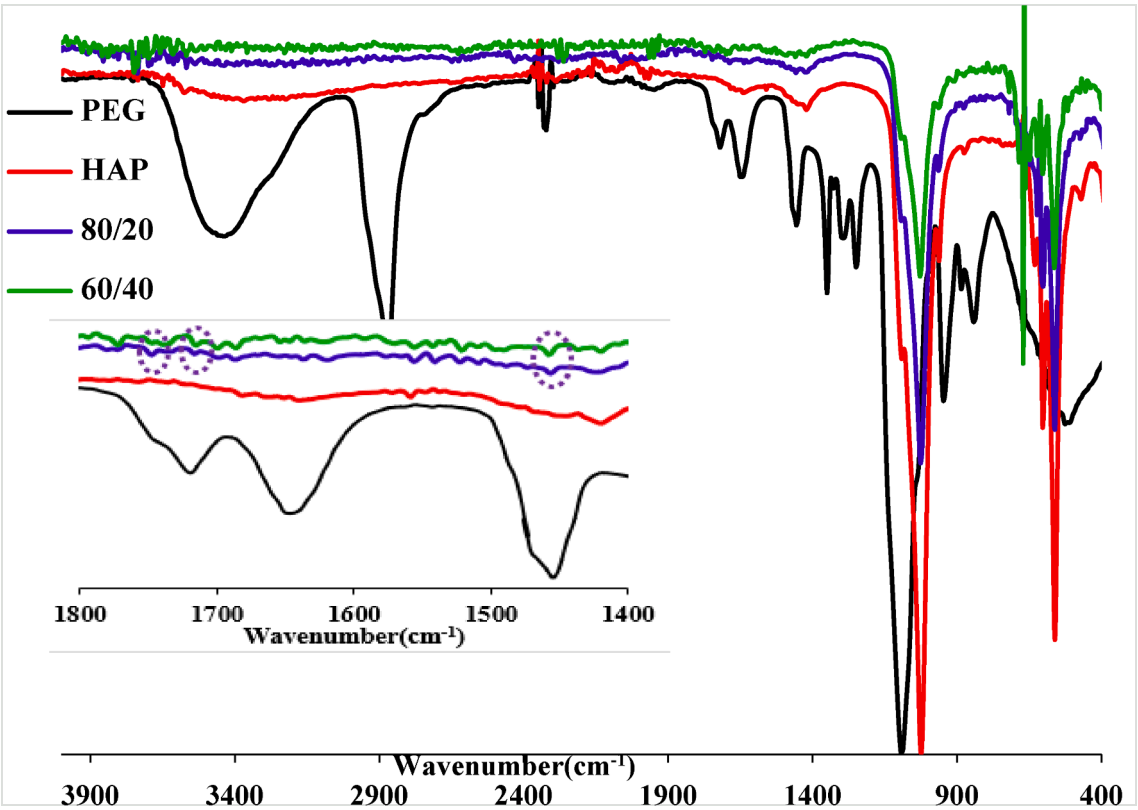

Fig. 3. ATR-FTIR spectra of HAP, PEG and mixed HAP/PEG (80/20 and 60/40).

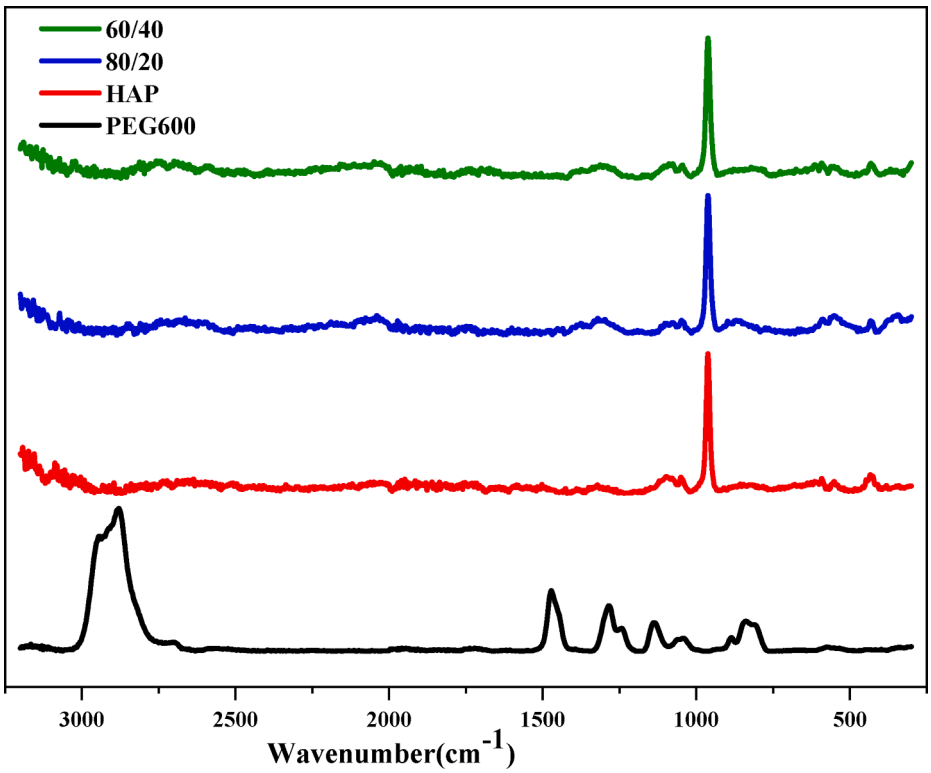

Fig. 4. Raman scattering spectra of pure HAP, pure PEG, and composite HAP/PEG (80/20 and 60/40).

indicates that PEG molecules have adsorbed onto the hydroxyapatite surface, forming a new complex.

The SEM analysis was used to investigate the surface morphology of the samples, as illustrated in Fig. 5-a. The SEM images reveal that both HAP and HAP/PEG particles exhibit a nearly spherical shape, with an average diameter of approximately 50 nm. Upon the addition of PEG,

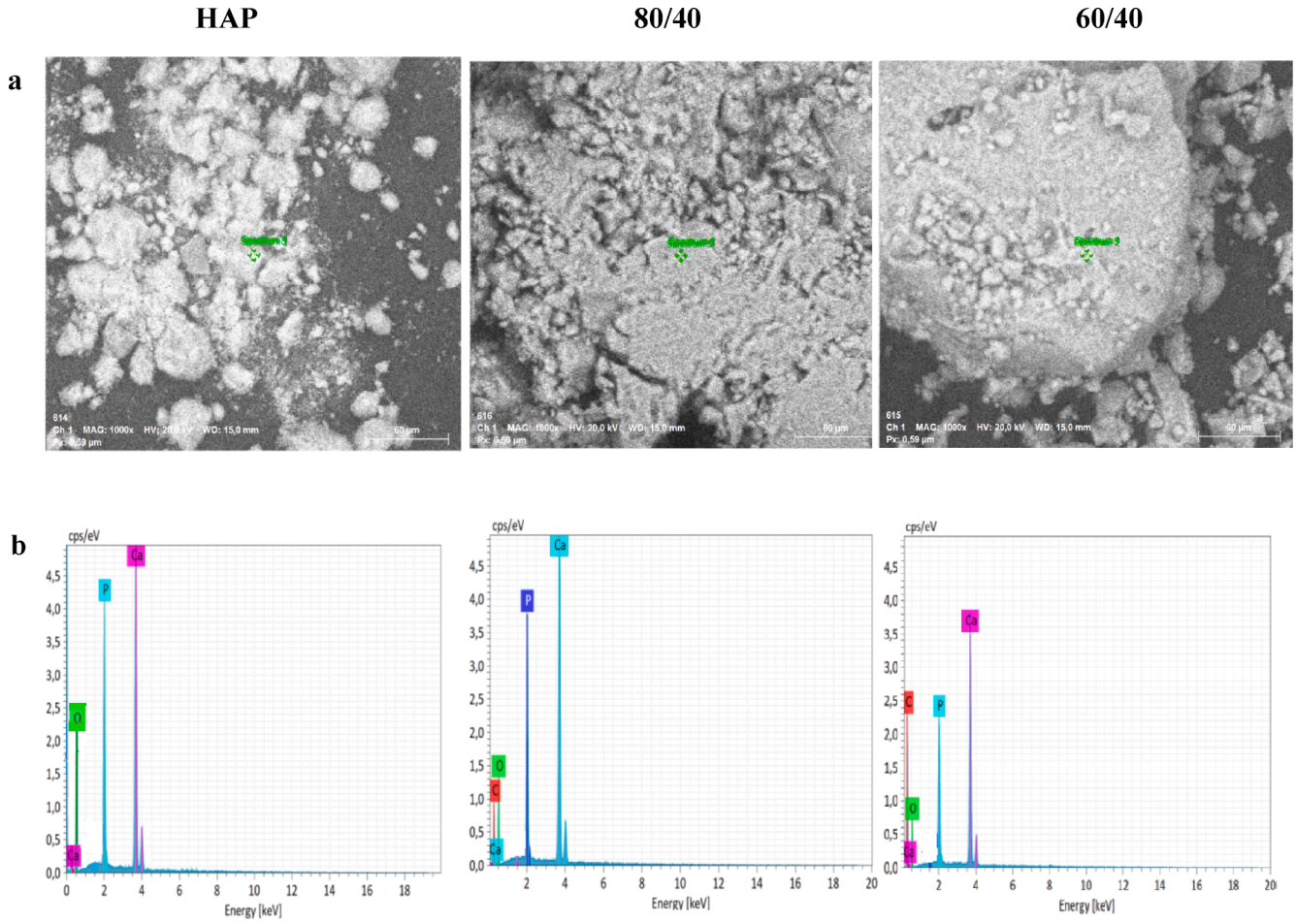

Fig. 5. SEM and EDS images of HAP, 80:20 and 60:40 composite.

the formation of PEG groups on the particle surfaces resulted in a steric effect that effectively prevented particle agglomeration. This can be attributed to the strong affinity between the inorganic crystals and the PEG polymer matrix, leading to an indistinguishable interface between the inorganic and organic phases. Notably, the SEM images demonstrate a transformation of the HAP particles into highly dispersed particles following the surface modification process. Furthermore, the elemental composition of the nanocomposite particles was investigated using energy dispersive spectroscopy (EDS), as shown in Fig. 5-b**.** The analysis confirmed the presence of calcium (Ca), phosphorus (P), and oxygen (O) elements in the obtained powder, aligning with the expected composition of HAP. Moreover, the elemental analysis of the HAP/PEG composite revealed the presence of carbon (C) because of the successful adhesion of PEG onto the HAP surface.

3.2. DFT calculation of the HAP/PEG nanocomposite

In addition to employing various experimental characterization techniques, this study incorporates a complementary theoretical investigation using density functional theory (DFT). The primary aim is to predict the precise structural model of the newly developed HAP/PEG hybrid material and comprehensively analyze its properties, including structural, optoelectronic, and chemical reactivity descriptors. This comprehensive investigation not only provides valuable insights into the nanocomposite's geometric characteristics, such as bond lengths and dihedral angles between atoms, but also enhances our understanding of its fundamental properties and potential applications. By combining experimental and theoretical approaches, this research contributes to advancing our knowledge of this exciting new material and its diverse range of properties.

3.2.1. Structural properties

Gaussian 09 software [28] was employed to optimize the molecular structure of the under investigated compound and the Gauss View (6) program [29] was used to generate the output files. Fig. 6 shown optimized geometry of the studied compound with the atom numbering. The main structural parameters of the compounds studied were determined through the DFT/B3LYP/6-31G (d, p) and ab-intio HF/3-21G methods, as outlined in Table 2.

The structural parameters of hydroxyapatite/polyethylene glycol hybrid material (HAP/PEG) were investigated in water solvent using the DFT calculation by the B3LYP method with the 6-31G (d, p) set and ab-intio Hartree Fock method with 3-21G basis set, in order to find the most stable geometry in the most suitable method and basis set. The choice of the suitable method and the basis set for this investigation were based mainly on the value of the calculated total energy. These values were evaluated in water solvent and gas phase using the CPCM model [30] in the different methods; DFT/B3LYP/6–31 G(d,p), and HF/3–21 (see Table 2)**.** It is obviously noted that the highest value was found with water as the solvent at both methods. In this section, all calculations were performed in solvent water with DFT/B3LYP/6-31G (d, p) level of theory. The structure of HAP/PEG compound with the atomic numbering schema is shown in Fig. 6. Its correspondent energy and its dipole moment at the DFT / B3LYP / 6-31G (d, p) and HF/3–21 levels of theory were found to be **−12859.83113/-12762.83113** Hartree, and **34.404134/26.984561** Debye, respectively.

Fig. 6 depicts the HAP/PEG hybrid material's optimized structure along with atomic labels and symbols. Table 3 lists the optimal bond

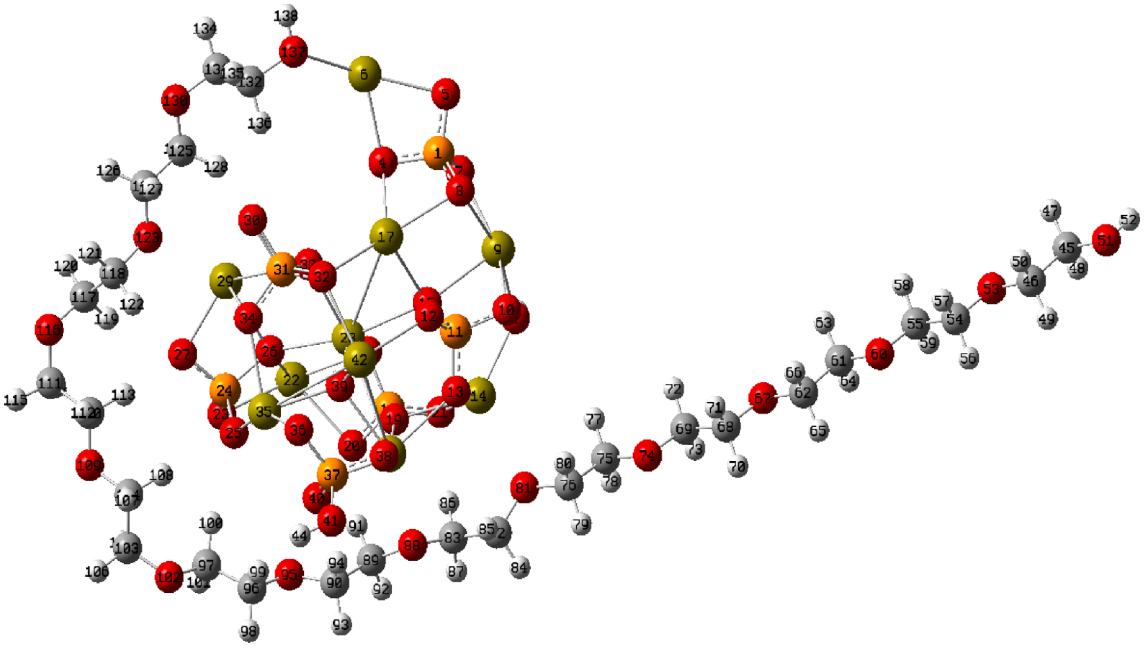

Fig. 6. Optimized ball-and-stick structural representation of the HAP/PEG hybrid material.

Table 2
Calculated total energy and dipole moments of hybrid material at DFT/B3LYP/ 6–31 g (d, p) and HF/3–21 methods in water in gas phase.

	DFT/B3LYP/6–31 G (d, p)		HF/3–21	
	Water	**Gas**	**Water**	**Gas**
Total Energy (Hartree)	**−12859.83113**	−12859.63243	**−12762.83113**	−12759.92724
Dipole Moment (Debye)	34.404134	29.39271	26.984561	20.715635

lengths, bond angles, and dihedral angles.

As clearly shown from the optimized structure, that there is a formation of new chemical liaison between the calcium atom (Ca6) of hydroxyapatite and the oxygen atom (O137) of polyethylene glycol, which can interpret as a chemical reaction between the two substances. It is well-known that the HAP has a high affinity for calcium ions and can form strong ionic bonds with them [31]. Therefore, in this case of HAP and PEG, the interaction is more likely to be dominated by ionic bonding between the calcium cation of HAP and the oxygen anion of PEG. This is because calcium and oxygen have significantly different electronigativities, which results in a large difference in their electron densities and strong attraction between them.

The bond lengths between calcium ions of HAP and oxygen of PEG are approximately equal to the sum of van der Waals radii of these atoms. As shown in Table 3, these bond lengths are in the range of 2.272 Å and 3.694 Å and correlated toto the theoretical bond lengths of the new chemical liaison Ca6–O137 (2.459 A) and the short contacts Ca42–O36, Ca 17–O33, Ca42–O 38, Ca and Ca17–O42which have bond lengths 2.560 Å, 2.562 Å, 2.566 Å, 2.601 Å, 2.704 Å, 2.898 Å and 3.694 Å respectively. As a result, the formation of calcium-oxygen bonds has been identified as an important driving force on the stabilization of the studied HAP/PEG hybrid material [32]. The hydroxyl radicals O2–H3 and O137–H138 linked to the Ca2 + ions undergo an ionic dissociation resulting in the production of OH − ions. The bond length values for these dissociated ions are 0.964 Å and 0.967 Å, respectively. These values presented herein are similar to the experimental structural data for hydroxyl radicals, which is about 0.970 Å [33]. In addition, the bond angle between Ca 6 -O 137 -H 138 is 119.22°, which is closely correlated with the bond angle between 110° and 180° on the electronic state of Ca-O–H [34]. The band angles O5-Ca6-O137, O38-Ca43-O88 and O2-Ca14-O81 are 125.72°, 122.49° and 124.70° respectively, which indicate that there is a deviation from the ideal bond angle for a trigonal planar geometry (120°).

The study and characterization of dihedral angles is a critical aspect of in understanding the properties and behavior of organic, bioorganic, nanoparticles, and hybrid materials [35]. The dihedral angles O15-Ca17-Ca29-O123, O7-Ca9-Ca14-O81, O33-Ca28-Ca43-O88, O2-Ca14-O81-C82, P24-o27-Ca29-O123, and O15-Ca9-Ca14-O81 are 177.85°, 164.41°, 163.66°, 179.76, −173.25°, −125. 63° respectively correspond to an anti-periplanar conformation with a shifted arrangement of the elements while the angles O15-Ca28-O123-C124, Ca35-Ca42-O88-C89, O12-Ca42-O88-Ca43 and O34-Ca35-Ca2-O32 are 7.07°, 5.79°, −3.93° and −2.78° respectively, which shows the synperplanar conformations.

3.2.2. Frontier molecular orbitals (FMOs) and global chemical reactivity descriptors properties

Frontier molecular orbitals (FMOs) and global chemical reactivity descriptors are important properties to consider when characterizing a hybrid material. FMOs are associated with the highest occupied molecular orbital (HOMO) and the lowest unoccupied molecular orbital (LUMO) and play an important role in determining the electronic and chemical properties of a materials. The HOMO is involved in electron-donating reactions, while the LUMO is involved in electron-accepting reactions. Therefore, the energy difference between the HOMO and LUMO, known as the band gap, plays a crucial role in establishing the optoelectronic characteristics of the studied materials, including its optical properties and conductivity [36]. Besides, Global chemical reactivity descriptors such as the electronegativity, chemical potential, and hardness of the material are also important in characterizing its properties [37]. The electronegativity represents the tendency of an atom to attract electrons, while the chemical potential describes the ability of the material to donate or accept electrons. Hardness represents

Table 3
Selected optimized bond lengths, bond angles and dihedral angles of the investigated compound.

Bond length		Bond Angle		Dihedral Angle	
O2-H3	0.964	P1-Ca6-O137	147.86	O8-Ca9-Ca14-O81	−108.5401
P1-Ca6	2.977	O4-Ca6-O137	121.38	O15-Ca9-Ca14-O81	−125.63
O4-Ca6	2.377	O5-Ca6-O137	125.72	Ca17-Ca9-Ca14-O81	−121.00
O5-Ca6	2.374	Ca9-Ca17-Ca42	111.37	Ca14-Ca9-O15-Ca28	−83.26
Ca6-O137	2.459	O12-Ca17-Ca28	79.46	O7-Ca9-Ca17-O32	152.80
Ca14-O19	2.476	O33-Ca17-Ca42	78.09	P11-O13-Ca43-O88	157.14
Ca14-O21	2.423	O21-P18-Ca22	138.07	Ca14-O13-Ca43-O88	43.54
Ca14-O81	2.704	Ca14-O19-Ca28	106.80	O81-Ca14-O19-P18	−107.70
Ca9-Ca14	3.875	P18-Ca22-O23	123.26	O81-Ca14-O19-Ca28	156.27
O4-H44	0.968	P18-Ca22-O28	53.41	O81-Ca14-O19-Ca43	63.17
O15-Ca28	2.515	O38-Ca42-O39	78.79	O81-Ca14-O21-P18	115.98
Ca17-Ca28	3.586	O13-Ca43-Ca38	90.53	O2-Ca14-O81-C82	179.76
Ca17-O33	2.562	O13-Ca43-Ca88	112.30	O13-Ca14-O81-C76	−73.65
Ca17-O42	3.694	O19-Ca43-Ca42	114.45	O13-Ca14-O81-C82	62.38
P18-Ca22	3.011	O19-Ca43-O88	77.15	O19-Ca14-O81-C76	−149.38
O19-Ca28	2.571	Ca28-Ca43-O38	115.38	O19-Ca14-O81-C82	−13.33
O137-H138	0.967	Ca28-Ca43-O88	121.36	O21-Ca14-O81-C76	148.13
Ca28-Ca29	3.767	O38-Ca43-O88	122.49	O21-Ca14-O81-C82	−75.81
Ca28-O33	2.468	O39-Ca43-O88	147.99	O4-Ca17-Ca29-O123	−81.87
Ca28-O39	2.272	Ca14-O81-C76	114.98	O8-Ca17-Ca29-O123	−107.94
Ca28-Ca43	3.543	Ca14-O81-C82	118.49	Ca9-Ca17-Ca29-O123	−151.27
Ca29-O33	2.572	Ca43-O88-C83	112.86	O12-Ca17-Ca29-O123	121.26
Ca29-O123	2.601	Ca43-O88-C89	108.41	O15-Ca17-Ca29-O123	177.85
O32-Ca42	2.401	Ca29-O123-C118	114.00	O32-Ca17-Ca29-O123	62.66
Ca35- Ca40	2.713	Ca29-O123-C124	124.923	Ca22-O26-Ca29-O123	79.27
Ca35- Ca42	3.477	O7-Ca9-Ca14	132.08	P24-O27-Ca29-O123	−173.25
O36- Ca42	2.560	C118-O123-C124	112.75	O15-Ca28-Ca43-O88	−111.81
O38- Ca42	2.566	Ca6-O137-C132	127.01	O16-Ca28-Ca43-O88	−14.52
O39-Ca43	2.261	Ca6-O137-H138	119.22	CA22-Ca28-Ca43-O88	25.17
Ca43-O88	2.893	O2-Ca14-O81	124.70	O26-Ca28-Ca43-O88	67.32
		Ca9-Ca14-O81	139.14	Ca29-Ca28-Ca43-O88	109.56
		O13-Ca14-O81	93.07	O33-Ca28-Ca43-O88	163.66
		O19-Ca14-O81	104.01	O15-Ca28-O123-C118	−129.71
		O21-Ca14-O81	99.36	O15-Ca28-O123-C124	7.07
		Ca9-O15-Ca28	144.64	O16-Ca28-O123-C118	107.46
		O4-Ca17-Ca42	163.19	O16-Ca28-O123-C124	−115.73
		O8-Ca17-O12	93.52	Ca17-Ca28-O123-C118	−121.73
		O8-Ca17-O15	79.34	Ca17-Ca28-O123-C124	15.05
		O8-Ca17-O28	118.36	O19-Ca28-O123-C118	36.29
		Ca9-Ca17-O12	76.72	O19-Ca28-O123-C124	173.09
		Ca9-Ca17-Ca28	80.52	Ca22-Ca28-O123-C118	84.39
		Ca9-Ca17-O32	150.61	Ca22-Ca28-O123-C124	−138.81
		Ca9-Ca17-O33	116.37	O39-Ca28-O123-C118	−37.07
				O39-Ca28-O123-C124	99.71
				Ca43-Ca28-O123-C118	−19.62
				Ca43-Ca28-O123-C124	117.16
				O33-Ca28-Ca43-O88	163.6641
				O123-Ca29-P31-O32	163.2469
				O5-Ca6-O137-H138	86.3672
				P1-O8-Ca17-Ca42	164.5527
				O7-Ca9-Ca14-O81	164.4172

the resistance of the material to chemical changes [38]. These descriptors can provide valuable insight into the chemical reactivity of the hybrid material, including its ability to undergo chemical reactions, its stability, and its potential applications. Overall, the characterization of FMOs and global chemical reactivity descriptors of a HAP/PEG hybrid material can provide crucial information for understanding its electronic and chemical properties, as well as for optimizing its performance for specific applications.

Table 4 lists the simulated values of frontier molecular orbitals (FMOs) energies and Global chemical reactivity descriptors of PEG, HAP and HAP/PEG hybrid materiel in the DFT/B3LYP/6–31 G (d, p) level of theory. Fig. 7 illustrates the FMOs of the nanocomposite under investigation, with particular emphasis on the HOMO orbital. This orbital is highlighted in red over the oxygen atoms in the –OH group of PEG, which are electronegative in nature. The HOMO orbital has an energy of −5.09 eV and the LUMO orbital with an energy of −0.47 eV. The highest value of the HOMO orbital is attributed to the oxygen electron donating groups, while the drop in LUMO value is due to the calcium atom

Table 4
Energy levels of frontier molecular orbitals (FMOs) and quantum chemical parameters global chemical reactivity descriptors obtained at DFT/B3LYP//6–31 g (d,p) for HAP, PEG and their corresponding HAP/PEG nanocomposite materiel.

	PEG600	HAP	HAP/PEG
ε_{HOMO} (eV)	−6.87	−5.55	−5.09
ε_{LUMO} (eV)	1.68	−4.24	−0.47
Energy band gap: Eg = $\Delta_{H\text{-}L}$ (eV)	8.56	1.30	**4.61**
Ionization potential: IP = - ε_{HOMO} (eV)	6.87	5.55	5.09
Electron affinity: EA = - ε_{LUMO} (eV)	−1.68	4.24	0.47
Chemical potential: $\mu = 1/2\ (\varepsilon_H + \varepsilon_L)$ (eV)	−2.59	−4.89	−2.78
Global hardness: $\eta = 1/2\ (\varepsilon_L - \varepsilon_H)$ (eV)	4.28	0.65	**2.30**
Global softness: $S = 1/(2\eta)$ (eV^{-1})	0.11	0.76	0.21
Electronegativity: $\chi = -1/2\ (\varepsilon_H + \varepsilon_L)$	−4.28	4.89	2.78
Global electrophilicity index:$\omega = \mu^2/2\ \eta$ (eV)	0.78	18.41	1.68
Maximum charge transfer index:$\Delta N_{Max} = -\mu/\eta$	0.60	7.51	1.20
Molecular stability: $\frac{\varepsilon_H}{\varepsilon_L}$	−4.08	1.30	**10.62**

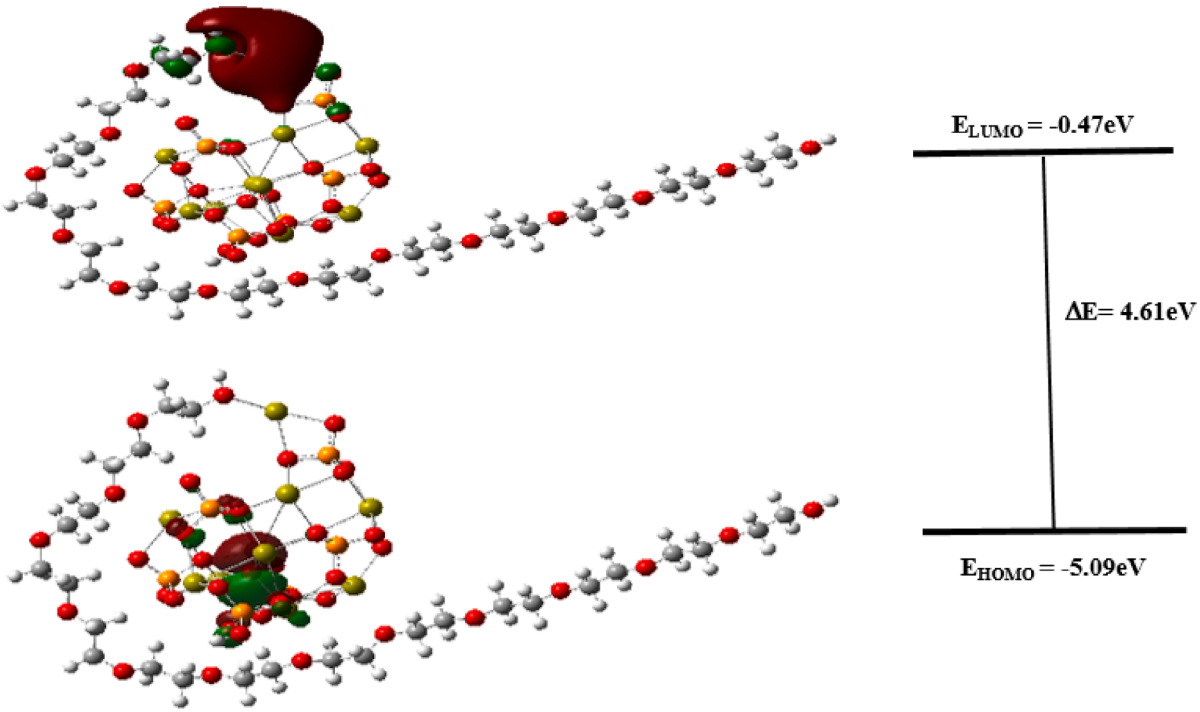

Fig. 7. FMOs distribution of Hydroxyapatite/ Polyethylene glycol compound at B3LYP/6-31G+ (d,p).

electron withdrawing groups.

The energy band gap plays a significant role in defining the electronic and optical characteristics of a studied system. As clearly seen in Table 4, the calculated bad energy gap of HAP/PEG hybrid materiel equal to 4.61 eV suggests that this material is a "Wide-band gap" semiconductor with potential applications in optoelectronics devices [39]. Compared to the individual components, the HAP/PEG nanocomposite has a larger band energy gap than HAP (1.30 eV) and a smaller band energy gap than PEG (8.56 eV). This implies that the electronic properties of the nanocomposite are different from those of its constituent materials. The composite material's band energy gap is increased by the addition of PEG to HAP, as seen by the higher band energy gap compared to HAP. This may be due to changes in the electronic structure and intermolecular interactions within the composite.

The global hardness parameter is an important descriptor of hybrid materiel's reactivity and stability. The computed global hardness (η) of the HAP/PEG hybrid material in our example is 2.30 eV, which is higher than that of HAP (0.65 eV) and lower than that of PEG (4.28 eV). This suggests that the nanocomposite is between the individual components in terms of reactivity and stability, and that it may have special chemical properties. The higher hardness value compared to HAP suggests that the hybrid materiel is more resistant to deformation and less likely to undergo chemical reactions. On the other hand, the lower hardness value compared to PEG suggests that the nanocomposite may have increased reactivity towards certain chemical species. These results indicate that the mixture between the fragile HAP (with a weak hardness value) and the rigid PEG (with a strong hardness value) results in a new nanocomposite with a good stiffness. The stability of a molecule depends on the energy gap between the HOMO and LUMO orbitals [40]. For the HAP/PEG nanocomposite, the $\mathbf{E_{HOMO}/E_{LUMO}}$ value of 10.62 indicates a relatively high level of molecular stability. Additionally, we observe that the investigated compound possesses a significant intermolecular charge transfer ability as indicated by the maximal charge transfer index, $\mathbf{\Delta N_{Max}}$ = 1.20 eV. All of these observations point to the potential for intramolecular interactions within our molecule, including Van der Waals and hydrogen-bonding interactions [41]. This value is a result of the HOMO and LUMO energy levels being relatively far apart, suggesting that the compound is less prone to undergo unwanted reactions or degradation processes. Overall, a high molecular stability is a desirable property for a nanocomposite, as it can lead to improved durability and longer functional lifetimes [42].

4. Conclusion

In conclusion, we successfully synthesized and characterized Hydroxyapatite/Polyethylene glycol (HAP/PEG) nanocomposite materials with two different ratios (80/20 and 60/20). The characterization techniques confirmed the formation of hybrid apatite materials. Through a combination of experimental and theoretical studies, we gained valuable insights into the properties of the HAP/PEG composite.

Our results revealed that the incorporation of t PEG with the fragile HAP led to the development of a nanocomposite material with enhanced hardness compared to pure HAP. This finding highlights the synergistic effect achieved by combining different materials, resulting in improved mechanical properties. Additionally, the HAP/PEG nanocomposite exhibited a high level of molecular stability, which further enhances its potential for various applications.

The integration of experimental characterization techniques and density functional theory (DFT) computational study provided a comprehensive understanding of the structural and mechanical aspects of the nanocomposite. This multidisciplinary approach not only allowed us to confirm the experimental observations but also provided valuable theoretical insights into the underlying mechanisms governing the properties of the composite.

CRediT authorship contribution statement

Dorsaf Bouazzi: Conceptualization, Methodology, Investigation, Writing – original draft. **Imen Chérif:** Conceptualization, Software, Methodology, Writing – original draft. **Afef Mehri:** Conceptualization, Methodology, Validation. **Houcine Touati:** Methodology, Investigation. **Maria Teresa Caccamo:** Resources, Investigation, Formal analysis, Validation. **Salvatore Magazù:** Investigation, Formal analysis, Resources. **Sahbi Ayachi:** Software, Investigation, Validation. **Jean-Marc**

Clacens: Resources, Investigation, Formal analysis. **Bechir Badraoui:** Project administration, Supervision.

Declaration of Competing Interest

The authors declare that they have no known competing financial interests or personal relationships that could have appeared to influence the work reported in this paper.

Data availability

Data will be made available on request.

Acknowledgements

This work was realized in the frame of the Programme ERASMUS + KA107, FE 2014/2020 P.O.R. Sicilia Project n° 2020-1-IT02-KA107-078488, and CUP J49J21003660006.

We thank the University of Monastir (Tunisia) for the continuous support during the realization of this work.

References

[1] S.D. Ratnasari, R.Y. Windari, N. Hidayat, Solid state reaction synthesis of Si-HA as potential biomedical material: An endeavor to enhance the added value of Indonesian mineral resources, IOP Conf. Series Mat. Sci. Eng. 202 (2017), 012021, https://doi.org/10.1088/1757-899X/202/1/012021.

[2] N.V. Bulina, M.V. Chaikina, I.Y. Prosanov, D.V. Dudina, L.A. Solovyov, Fast synthesis of La-substituted apatite by the dry mechanochemical method and analysis of its structure, J. Solid-State Chem. 252 (2017) 93–99, https://doi.org/10.1016/j.jssc.2017.05.008.

[3] P.N. Lim, T. Konishi, Z. Wang, J. Feng, L. Wang, J. Han, Z. Yang, E.S. Thian, Enhancing osteoconductivity and biocompatibility of silver-substituted apatite in vivo through silicon co-substitution, Mat. Lett. 212 (2018) 90–93, https://doi.org/10.1016/j.matlet.2017.10.076.

[4] E.N. Yudyanto, N.M. Azizah, N. Hartatiek, R.K. Hidayat, Effect of stirring duration on hardness and antibacterial characteristics of Polyethylene Glycol-Hydroxyapatite nanocomposites, IOP Conf. Series Mat. Sci. Eng. 515 (2019), 012073, https://doi.org/10.1088/1757-899X/515/1/012073.

[5] R.N. Granito, A.C. Muniz Renno, H. Yamamura, M.C. de Almeida, P.L. Menin Ruiz, D.A. Ribeiro, Hydroxyapatite from fish for bone tissue engineering: A promising approach, Int. J, of Mol. Cell. Med. 7 (2018) 80–90, https://doi.org/10.22088/IJMCM.BUMS.7.2.80.

[6] J. Hartatiek, I.N. Utomo, R. Lisdiana, Nur Zaidatur, Physical and mechanical properties of hydroxyapatite/polyethylene glycol nanocomposites, Mat. Today Proc. 44 (2021) 3263–3267, https://doi.org/10.1016/j.matpr.2020.11.511.

[7] Y. Abe, Y. Okazaki, K. Hiasa, K. Yasuda, K. Nogami, W. Mizumachi, I. Hirata, Bioactive surface modification of hydroxyapatite, Biomed Res. Int. 2013 (2013), 626452, https://doi.org/10.1155/2013/626452.

[8] P. He, S. Sahoo, K. Siang Ng, K. Chen, S. Lok Toh, J. Cho Hong Goh, Enhanced osteoinductivity and osteoconductivity through hydroxyapatite coating of silk-based tissue-engineered ligament scaffold, J. biom. Mat. Res. A 101 (2013) 555–566, https://doi.org/10.1002/jbm.a.34333.

[9] M. Salah, L. Tayebi, K. Moharamzadeh, F.B. Naini, Three-dimensional bio-printing and bone tissue engineering: technical innovations and potential applications in maxillofacial reconstructive surgery, Maxillo plastic reconstr. surgery 42 (2020) 1–9, https://doi.org/10.1186/s40902-020-00263-6.

[10] C. Albano, R. Perera, L. Cataño, A. Karam, G. González, Prediction of mechanical properties of composites of HDPE/HA/EAA, J. Mech. Beh. Biom. Mat. 4 (2011) 467–475, https://doi.org/10.1016/j.jmbbm.2010.12.008.

[11] A. Sharma, G.R. Kokil, Y. He, B. Lowe, A. Salam, T.A. Altalhi, Q. Ye, T. Kumeria, Inorganic/organic combination: Inorganic particles/polymer composites for tissue engineering applications, J. Bioactive Materials. 4 (2023) 535–550, https://doi.org/10.1016/j.bioactmat.2023.01.003.

[12] J. Zhang, W. Fang, Z. Liu, R. Tang, Inorganic ionic polymerization: A bioinspired strategy for material preparation, J. Biogeotechnics 1 (2023), 100004, https://doi.org/10.1016/j.bgtech.2023.100004.

[13] J.A. Lett, S. Sagadevan, I. Fatimah, et al., Recent advances in natural polymer-based hydroxyapatite scaffolds: Properties and applications, Eur. Polym. J. 148 (2021), 110360, https://doi.org/10.1016/j.eurpolymj.2021.110360.

[14] C.P. Dhanalakshmi, L. Vijayalakshmi, V. Narayanan, Synthesis and Preliminary Characterization of Polyethylene Glycol (PEG)/Hydroxyapatite (HAp) Nanocomposite for Biomedical Applications, Int. J. Phys. Sci. 7 (2012) 2093–2101, https://doi.org/10.5897/IJPS11.1495.

[15] S. Jegatheeswaran, M. Sundrarajan, PEGylation of novel hydroxyapatite/PEG/Ag nanocomposite particles to improve its antibacterial efficacy, Mat. Sci. Eng. C 51 (2015) 174–181, https://doi.org/10.1016/j.msec.2015.02.012.

[16] Z. Peng, C. Ji, Y. Zho, T. Zhao, R.M. Leblanc, Polyethylene glycol (PEG) derived carbon dots: Preparation and applications, Appl. Mat. Today 20 (2020), 100677, https://doi.org/10.1016/j.apmt.2020.100677.

[17] S. Ranganathan, B. Kalimuthu, S. Nagarajan, Chitosan and gelatin-based electrospun fibers for bone tissue engineering, Intern. J. Biol. Macromol. 133 (2019) 354–364, https://doi.org/10.1016/j.ijbiomac.2019.04.115.

[18] A.D. Becke, Density-functional thermochemistry. III. The role of exact exchange, J. Chem. Phys. 98 (1993) 5648–5652, https://doi.org/10.1063/1.464913.

[19] D. Bouazzi, A. Mehri, K. Kaaroud, H. Touati, F. Karouia, J.M. Clacens, A. Laghzizil, B. Badraoui, Beneficial effect of in-situ citrate-grafting of hydroxyapatite surface for water treatment, Coll. Surf. A Physicochem. Eng. Aspects 666 (2023), 131366, https://doi.org/10.1016/j.colsurfa.2023.131366.

[20] A.D. Becke, Density-functional thermochemistry. IV. A new dynamical correlation functional and implications for exact-exchange mixing, J. Chem. Phys. 104 (1996) 1040–1046, https://doi.org/10.1063/1.470829.

[21] C. Lee, W. Yang, R.G. Parr, Development of the Colle-Salvetti correlation-energy formula into a functional of the electron density, Phys. Rev. B 37 (1988) 785–789, https://doi.org/10.1103/PhysRevB.37.785.

[22] J.R. Cheeseman, et al., Hartree− Fock and density functional theory ab initio calculation of optical rotation using GIAOs: basis set dependence, Chem. A Eur. J. 104 (5) (2000) 1039–1046, https://doi.org/10.1063/1.470829.

[23] Y. Yang, et al., Synthesis of aligned porous polyethylene glycol/silk fibroin/hydroxyapatite scaffolds for osteoinduction in bone tissue engineering, Stem Cell Res Ther 11 (2020) 1–17, https://doi.org/10.1186/s13287-020-02024-8.

[24] Y. Deng, J. Li, T. Qian, W. Guan, Y. Li, X. Yin, Thermal conductivity enhancement of polyethylene glycol/expanded vermiculite shape-stabilized composite phase change materials with silver nanowire for thermal energy storage, Chem. Eng. J. 295 (2016) 427–435, https://doi.org/10.1016/j.cej.2016.03.068.

[25] Y. Yingkai, W. Wang, Y. Zhan, C. Zheng, G. Wang, A simple route to hydroxyapatite nanofibers, Mat. Lett. 56 (2002) 496–501, https://doi.org/10.1016/S0167-577X(02)00539-6.

[26] T. Haoliang, W. Tian, G. Changliang, C. Mengqiu, G. Yongjing, T. Junguo, L. Zhihui, S. Yi, W. Cong, J. Hao, W. Guo, Shicheng, Study on process and performance of thermal protective coating on polyimide resin matrix composite, Ceram. Intern. 46 (2020) 12744–12758, https://doi.org/10.1016/j.ceramint.2017.11.120.

[27] D. Yamini, G. Devanand Venkatasubbu, J. Kumar, V. Ramakrishnan, Raman scattering studies on PEG functionalized hydroxyapatite nanoparticles, Spectr. Acta Part A: Mol. Biomol. Spectr. 117 (2014) 299–303, https://doi.org/10.1016/j.saa.2013.07.064.

[28] M.J. Frisch, et al., Gaussian 09, revision A.01, Gaussian Inc, Wallingford, 2009.

[29] GaussView, Version 6.0, Roy Dennington, Todd A. Keith, and John M. Millam, Semichem Inc., Shawnee Mission, KS, 2016.

[30] V. Mishra, A. Raghuvanshi, A. Kumar Saini, S.M. Mobin, Anthracene derived dinuclear gold (I) diacetylide complexes: Synthesis, photophysical properties and supramolecular interactions, J. Organometal. Chem. 813 (2016) 103–109, https://doi.org/10.1016/j.jorganchem.2016.04.013.

[31] A. Ressler, A. Žužić, I. Ivanišević, N. Kamboj, H. Ivanković, Ionic substituted hydroxyapatite for bone regeneration applications: A review, Open Ceram. 6 (2021), 100122, https://doi.org/10.1016/j.oceram.2021.100122.

[32] C. Gervais, et al., New perspectives on calcium environments in inorganic materials containing calcium–oxygen bonds: a combined computational–experimental 43Ca NMR approach, Chem. Phys. Lett. 464 (2008) 42–48, https://doi.org/10.1016/j.cplett.2008.09.004.

[33] P. Batra, R. Gabam, U. Issar, R. Kakkar, Structures and stabilities of alkaline earth metal oxide nanoclusters: a DFT study, J. Theor. Chem. 2013 (2013), 720794, https://doi.org/10.1155/2013/720794.

[34] Z. Mohammadi, P.M. Howell Dummer, Properties and applications of calcium hydroxide in endodontics and dental traumatology, Intern. Endod. J. 44 (2011) 697–730, https://doi.org/10.1111/j.1365-2591.2011.01886.x.

[35] P. Hansia, G. Nandini, V. Saraswathi, Ab initio studies on the tri-and diphosphate fragments of adenosine triphosphate, Biophys. Chem. 119 (2006) 127–136, https://doi.org/10.1016/j.bpc.2005.07.011.

[36] I. Chérif, H. Raissi, K. Abiedh, B. Gassoumi, M.T. Caccamo, S. Magazù, A. Haj Said, F. Hassen, T. Boubaker, S. Ayachi, Exploration of intramolecular charge transfer in para-substituted nitrobenzofurazan: Experimental and theoretical analyses, Spectrochim. Acta Part A Mol. Biom. Spectr. 301 (2023) 1386–1425, https://doi.org/10.1016/j.saa.2023.122939.

[37] J.R. Durig, T.S. Little, T.K. Gounev, J.K. Gardner Jr., J.F. Sullivan, Infrared and Raman spectra, conformational stability, vibrational assignment, and ab initio calculations of chloromethyl isocyanate, J. Mol. Struct. 375 (1996) 83–94, https://doi.org/10.1016/0022-2860(95)08983-7.

[38] M. Yoosefian, A. Zahra, E. Nazanin, Density functional theory computational study on solvent effect, molecular conformations, energies and intramolecular hydrogen bond strength in different possible nano-conformers of acetaminophen, J. Mol. Liquids 213 (2016) 115–121, https://doi.org/10.1016/j.molliq.2015.10.060.

[39] C.S. Liu, X. Le Yang, J. Liu, X.J. Ye, Exfoliated monolayer GeI2: theoretical prediction of a wide-band gap semiconductor with tunable half-metallic ferromagnetism, J. Phys. Chem. C 122 (2018) 22137–22142, https://doi.org/10.1021/acs.jpcc.8b05529.

[40] L. Anitha, S.R. Saritha, S.R. Layana, C.S. Nair Lakshmi, I. Hubert Joe, M. R. Sudarsanakumar, Structural studies of 3-[(E)-[(2E)-2-methyl-3-phenylprop-2-en-1-ylidene] amino]-1-phenylthiourea: Combined experimental and

computational studies, J. Mol. Struct. 1191 (2019) 206–217, https://doi.org/10.1016/j.molstruc.2019.04.062.
[41] I. Chérif, H. Raissi, et al., Photophysical and nonlinear optical properties of para-substituted nitrobenzofurazan: A comprehensive DFT investigation, J. Photochem. Photobiol. A Chem. 443 (2023), 114850.
[42] Q. Chen, et al., Under the spotlight: The organic–inorganic hybrid halide perovskite for optoelectronic applications, Nano Today 10 (2015) 355–396, https://doi.org/10.1016/j.nantod.2015.04.009.